GFZ

Helmholtz-Zentrum
POTSDAM

Originally published as:

RESEARCH ARTICLE

Ensemble simulations of the magnetic field induced by global ocean circulation: Estimating the uncertainty

Christopher Irrgang[1,2], Jan Saynisch[1], and Maik Thomas[1,2]

[1]Helmholtz Centre Potsdam, GFZ German Research Centre for Geosciences, Section 1.3: Earth System Modelling, Potsdam, Germany, [2]Freie Universität Berlin, Institute of Meteorology, Berlin, Germany

Abstract The modeling of the ocean global circulation induced magnetic field is affected by various uncertainties that originate from errors in the input data and from the model itself. The amount of aggregated uncertainties and their effect on the modeling of electromagnetic induction in the ocean is unknown. For many applications, however, the knowledge of uncertainties in the modeling is essential. To investigate the uncertainty in the modeling of motional induction at the sea surface, simulation experiments are performed on the basis of different error scenarios and error covariance matrices. For these error scenarios, ensembles of an ocean general circulation model and an electromagnetic induction model are generated. This ensemble-based approach allows to estimate both the spatial distribution and temporal variation of the uncertainty in the ocean-induced magnetic field. The largest uncertainty in the ocean-induced magnetic field occurs in the area of the Antarctic Circumpolar Current. Local maxima reach values of up to 0.7 nT. The estimated global annual mean uncertainty in the ocean-induced magnetic field ranges from 0.1 to 0.4 nT. The relative amount of uncertainty reaches up to 30% of the signal strength with largest values in regions in the northern hemisphere. The major source of uncertainty is found to be introduced by wind stress from the atmospheric forcing of the ocean model. In addition, the temporal evolution of the uncertainty in the induced magnetic field shows distinct seasonal variations. Specific regions are identified which are robust with respect to the introduced uncertainties.

1. Introduction

Ocean circulation generates characteristic electromagnetic signals, as the moving salt ions interact with the ambient geomagnetic field. The so-called motionally induced magnetic field is to first order proportional to the conductivity-weighted and depth-integrated ocean velocities [*Sanford*, 1971]. This provides the opportunity to indirectly observe ocean global circulation by measuring the ocean circulation induced magnetic field (e.g., by satellites). Several studies cover the theoretical aspects of the oceanic induced electromagnetic fields, such as *Larsen* [1968], *Sanford* [1971], *Cox* [1980], *Chave* [1983], and *Chave and Luther* [1990]. In more recent studies, the focus is to estimate the strength and the patterns of the motionally induced magnetic field by utilizing ocean models. The modeling of motional induction due to ocean circulation (global and regional) is investigated by, e.g., *Stephenson and Bryan* [1992], *Flosadóttir et al.* [1997], *Tyler et al.* [1997], *Vivier et al.* [2004], and *Manoj et al.* [2006]. In further studies, motional induction due to tidal motion is addressed, e.g., by *Tyler et al.* [2003], *Maus and Kuvshinov* [2004], *Kuvshinov et al.* [2006], *Dostal et al.* [2012], *Schnepf et al.* [2014, 2015], and *Sabaka et al.* [2015]. *Irrgang et al.* [2016] investigate the influence of spatial and temporal variations of seawater conductivity on motional induction due to ocean circulation. The sensitivity experiments demonstrate the need to account for a realistic seawater conductivity distribution. However, the robustness of model-based results of motional induction, i.e., the influence of uncertainties in the modeling approach, has not yet been investigated. Any application of motional induction, e.g., the comparison of model results with observations, feasibility studies, or data assimilation, is only valid if the uncertainty is well characterized [e.g., *Evensen*, 1994]. Uncertainties in the modeling approach can arise from errors in the input data, as well as from errors in the simulation itself. Errors occur due to simplified physics and numerical schemes. Atmospheric forcing reanalysis products are provided by several centers. The discrepancies between the different reanalysis products were analyzed in several recent studies, e.g., *Jakobson et al.* [2012], *Decker et al.* [2012], *Chaudhuri et al.* [2013], and *Kim and Alexander* [2013]. Particularly, wind stress and precipitation fields show nonnegligible discrepancies that can result in large uncertainties in the ocean

circulation [*Chaudhuri et al.*, 2013]. Consequently, the magnetic field, which is induced by ocean circulation, also contains errors due to atmospheric forcing. Additional uncertainties are introduced by errors in the ambient geomagnetic field and in the sediment conductivity, which also arise due to varying modeling approaches [see e.g., *Lowes*, 2000; *Thébault et al.*, 2015] or the application of heuristic methods [e.g., *Everett et al.*, 2003], respectively. Uncertainties in the modeling of the conductivity structure underneath the ocean and oceanic sediments may also influence the modeling of ocean-induced magnetic signals. However, due to the model approach used in this study (see section 2.1.2), the source of uncertainty in the mantle of the Earth is not considered in this study.

In this paper, the robustness of modeling the motionally induced magnetic field is systematically studied by investigating the influence of uncertainties in the modeling approach. This is accomplished by performing a set of ensemble simulations that incorporate different scenarios for error approximations. In this paper, the motionally induced magnetic field is calculated by coupling an ocean global circulation model and an electromagnetic induction model (see section 2.1). The combination of these two models was already used by *Irrgang et al.* [2016] and builds the basis for the ensemble experiments in this study. In particular, the focus of this study lies on magnetic signals, which originate from large-scale ocean circulation patterns and which are apparent at both sea surface and satellite altitude. Both models utilize additional input data, i.e., atmospheric forcing, ambient geomagnetic field, and oceanic sediment conductivity (see section 2.1). The intermediate objectives of this study are (1) the approximation of the major introduced error budgets by error covariance matrices, (2) the calculation of the aggregated uncertainty in the modeling of motional induction, and (3) the identification of spatiotemporal patterns in the motionally induced magnetic field that are robust with respect to introduced uncertainties.

This paper is structured as follows. In section 2, the ocean model and the electromagnetic induction model are described. The setup of the ensemble simulations and the utilized data are depicted and the experiment design is explained (objective 1). The results are presented and discussed in section 3 (objectives 2 and 3). A summary and final conclusions are given in section 4.

2. Methodology

2.1. Model Setup

2.1.1. Global Ocean Model

The global ocean circulation is modeled with the Ocean Model for Circulation and Tides (OMCT) [*Thomas et al.*, 2001]. OMCT is a baroclinic model which incorporates nonlinear balance equations for momentum, the continuity equation, and conservation equations for heat and salt. A resolution of $1.875°$ in longitude and latitude and 13 layers in the vertical are used. The time stepping is set to 30 min. Additionally, the Boussinesq and the hydrostatic approximations are applied. Artificial mass changes due to the Boussinesq approximation are corrected, as suggested by *Greatbatch* [1994]. The model is forced with heat-flux, wind stress, surface-pressure, precipitation, and evaporation. The forcing is provided by 6-hourly ERA-Interim reanalysis products from the European Centre for Medium-Range Weather Forecasts (ECMWF) [*Dee et al.*, 2011]. Since this study focuses on motional induction due to ocean circulation, ocean tides are not considered in this configuration of the OMCT.

The OMCT is used in several studies [e.g., *Dobslaw and Thomas*, 2007; *Dostal et al.*, 2012; *Dobslaw et al.*, 2013; *Saynisch et al.*, 2014; *Irrgang et al.*, 2016] and is considered to realistically resolve the main features of ocean global circulation. In the current configuration, the OMCT does not resolve small-scale features, which also affect motional induction in the ocean [e.g., *Lilley et al.*, 1993]. However, due to smoothing effects by the upwardly continuation to satellite altitude, small-scale features that are visible in the motionally induced magnetic field at sea surface are blurred with increasing height [*Vennerstrom et al.*, 2005; *Manoj et al.*, 2006]. Therefore, the used resolution is justifiable, since the focus of this study lies on the large-scale features that are apparent at both sea surface and satellite altitude.

2.1.2. Electromagnetic Induction Model

The electromagnetic induction model calculates the radial component of the primary motionally induced poloidal magnetic field. The poloidal component of the motionally induced magnetic field reaches outside the ocean and can be calculated at sea surface and satellite altitude. The focus of this study solely lies on the oceanic induced magnetic signals, which directly originate from large-scale ocean global circulation

and which can, in principle, be measured outside the ocean. Therefore, the primary toroidal component of the oceanic induced magnetic field is not considered in this study, as it is confined to the ocean. Likewise, secondary poloidal magnetic signals, which are generated by coupling effects of the primary toroidal signal and large conductivity contrasts at continental borders [*Dostal et al.*, 2012; *Szuts*, 2010], are not considered.

The model utilizes a 2-D induction equation and follows a similar approach as described in *Vivier et al.* [2004] and *Tyler et al.* [1997]. The ocean basin is approximated by a thin horizontal shell which contains conductivity-weighted and subsequently depth-integrated horizontal ocean flow velocities. Vertical ocean flow velocities are neglected. The atmosphere and upper mantle are treated as insulators [*Vivier et al.*, 2004; *Parkinson and Hutton*, 1989]. The thin shell is allowed to include an underlying layer of conductive sediments. Therefore, a global sediment conductance map has been derived using the method described by *Everett et al.* [2003] and sediment thicknesses obtained from *Laske and Masters* [1997]. Based on Ampere's Law and Ohm's Law, the induced electric currents in the thin shell are given by an electric stream function ψ_e, which leads to a scalar model equation [*Vivier et al.*, 2004]:

$$\nabla \cdot \left(\Sigma^{-1} \nabla \psi_e \right) = \nabla \cdot \left(\Sigma^{-1} F_z \int_h \sigma \boldsymbol{u}_H dz \right). \tag{1}$$

Here h is the variable height of the thin shell according to the bathymetry, Σ is the depth-integrated conductivity of the water column and underlying sediments, σ is the conductivity at a given point (ϕ, ϑ, z), F_z is the radial part of the ambient geomagnetic field, and $\boldsymbol{u}_H$ is the horizontal ocean flow velocity. F_z is derived from the POMME-6 Magnetic Model of the Earth [*Maus et al.*, 2010] and $\boldsymbol{u}_H$ is prognostically calculated with the OMCT. The poloidal oceanic induced magnetic field b_r is derived from the stream function ψ_e using spherical harmonic expansion:

$$b_r(\phi, \vartheta, r) = \sum_{j=0}^{j_{\max}} \sum_{m=-j}^{j} \frac{1}{2} \frac{\mu_0}{r} \psi_{jm} \left(\frac{a}{r} \right)^{j+1} (j+1) Y_{jm}(\phi, \vartheta). \tag{2}$$

Here ϕ and ϑ are longitudinal and colatitudinal coordinates on the sphere, μ_0 is the permeability of free space, a is the Earth's radius, r is the height above sea level, and ψ_{jm} and $Y_{jm}(\phi, \vartheta)$ are the spherical harmonic coefficients and functions. The indices j and m are degree and order of the spherical harmonics. The spherical harmonic coefficients are calculated as described by *Driscoll and Healy* [1994]. The degree and order of the spherical harmonic expansion $j_{\max}$ is limited to 47, in order to prevent aliasing effects due to grid transformations [*Driscoll and Healy*, 1994].

2.2. Ensemble Simulations

The input data that are utilized to initialize and force the two described models contain uncertainty and error correlation. The sources of these uncertainties are manifold and affect both the initial state of the model and the trajectory of the model. To estimate these uncertainties and their effect on the motionally induced magnetic field, an ensemble-based model approach is carried out, as suggested by *Evensen* [1994]. The ensemble members, i.e., the model realizations, differ from each other by the initial OMCT model state x_0, wind stress, geomagnetic field, and sediment conductance (see Figure 1). The spread of the ensemble, i.e., the cross-ensemble variance, arises due to these different initial states and the respective response of the model dynamics to the forcings. The analysis of the ensemble spread allows to quantify amount, spatial patterns, and the temporal evolution of the uncertainty of the motionally induced magnetic field.

The ensemble and its initial spread are generated from the initial model error, which is represented by the error covariance matrix P_0. Since the error covariance matrix of an ocean general circulation model (OGCM) is high-dimensional, a reduced-rank approximation of the error covariance matrix P_0 (in decomposed form) is utilized, i.e.,

$$\tilde{P}_0 := V_0 U_0 V_0^T \approx P_0. \tag{3}$$

This low-rank approximation only considers the r largest eigenmodes of the covariance matrix P_0. More specifically, an error subspace is defined by the most significant directions of uncertainty [*Nerger et al.*, 2005]. Consequently, the $r \times r$ diagonal matrix U_0 contains the r largest eigenvalues of P_0 and the $n \times r$ matrix V_0 contains the corresponding eigenvectors. This projection onto an error subspace allows the usage of (usually) much smaller ensemble sizes to sample P_0 realistically [*Nerger et al.*, 2007]. Consequently, an ensemble
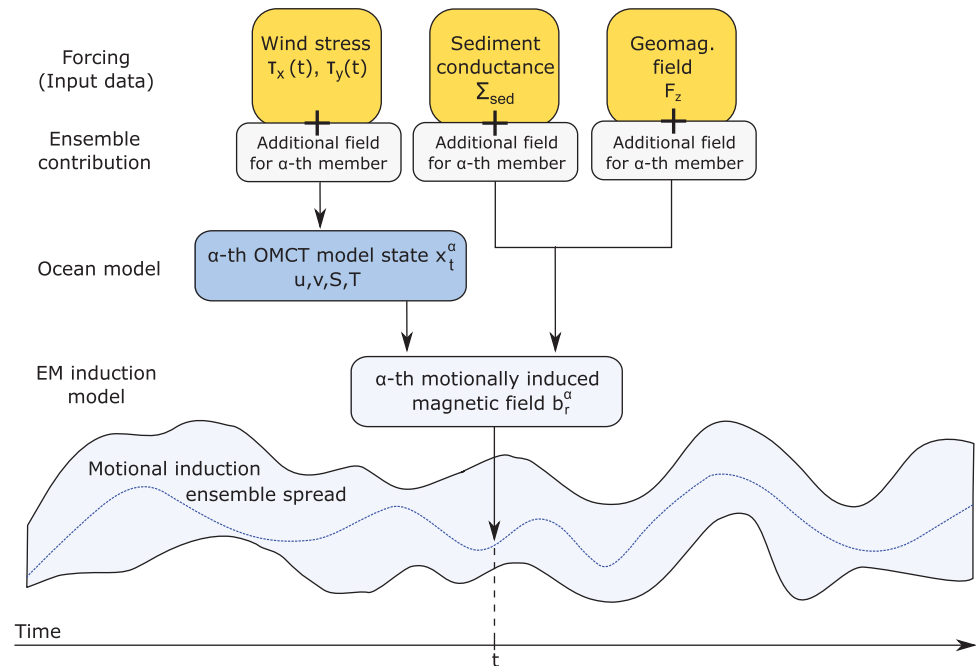
Figure 1. Sketch of the ensemble simulation setup.

$\{x_0^1, \ldots, x_0^{r+1}\}$ of minimum size is generated from the r largest eigenmodes by second-order exact sampling [*Pham*, 2001]:

$$x_0^{\alpha} = x_0 + \sqrt{r+1}\, V_0 C_0^T (\Omega_0^T)^{(\alpha)}, \tag{4}$$

for $\alpha = 1, \ldots, r+1$. The matrix C_0 is chosen such that $U_0 = C_0^T C_0$ and Ω_0 is a $(r+1) \times r$ random matrix chosen such that the columns are orthonormal to each other and orthogonal to the vector $(1, \ldots, 1)^T$. $(\Omega_0^T)^{(\alpha)}$ is the αth column of Ω_0^T. This construction ensures that the statistics of the ensemble replicate the initial model error (in second-order exact sense), i.e.,

$$\tilde{P}_0 = \frac{1}{r+1} \sum_{\alpha=1}^{r+1} (x_0^{\alpha} - \overline{x_0^{\alpha}})(x_0^{\alpha} - \overline{x_0^{\alpha}})^T. \tag{5}$$

The cross-ensemble mean $\overline{x_0^{\alpha}}$ represents the best estimate of the model state. The notation of the ensemble generation follows *Nerger et al.* [2005], who also provide additional information on the mathematical background.

This approach leads to a systematically generated ensemble of model trajectories (see Figure 1). In this study, an ensemble size of 16 is used. Larger ensemble sizes did not change the results. The state vector x_0 is chosen to consist of the following components that are (directly and indirectly) necessary to calculate the motionally induced magnetic field (cf. equation (1)): 3D-fields of zonal ocean flow velocity u, meridional ocean flow velocity v, salinity S, ocean temperature T; and 2D-fields of zonal wind stress τ_x, meridional wind stress τ_y, radial component of the ambient geomagnetic field F_z, and oceanic sediment conductance Σ_{sed} (as a part of Σ). The components u, v, S, and T are dynamically simulated with the OMCT, whereas τ_x, τ_y, F_z, and Σ_{sed} are added via input data. τ_x, τ_y, F_z, and Σ_{sed} are included in the state vector to account for errors in the input data. The forcings (τ_x, τ_y, F_z, and Σ_{sed}) of all ensemble members differ according to equation (4). Consequently, a specific field (depending on the error scenario) is added to the read-in forcings for each ensemble member (see yellow boxes in Figure 1 and *Saynisch et al.* [2014]). τ_x, τ_y, and their errors are assumed to vary in time, whereas F_z, Σ_{sed}, and their errors are assumed to be constant in time. The initial state of each ensemble member is propagated through time with the full nonlinear ocean model and the respective forcings (dark blue box in Figure 1). The initial variance, i.e., the initial spread, of this ensemble equals (in second-order exact sense) to the prescribed uncertainties in P_0 (see error scenarios in the

following section). Note that due to the nonlinearity and internal dynamics of the ocean model, even small differences between the initial state of two ensemble members can eventually lead to very large differences between the two trajectories.

2.3. Experiment Design

The truncated error covariance matrix $\tilde{P}_0$ characterizes the main uncertainties in the input data and in the initial state of the ocean model. The estimation of realistic values for $\tilde{P}_0$ is a challenge. Therefore, three experiments with different error scenarios, i.e., different error covariance matrices, are performed over the simulation period of 1 year. The wind stress forcing has deficiencies on spatial and temporal scales. Compared to the wind stress values, the errors easily exceed 20% and often reach maxima as large as the modeled stress itself [*Chaudhuri et al.*, 2013]. It is expected to introduce a major source of (temporally variable) error [see also *Saynisch et al.*, 2014].

The first experiment is called ONE-FORC. In ONE-FORC, it is assumed that eventually the atmospheric forcing can be completely wrong. The temporal covariances are calculated from the ERA-Interim atmospheric forcing data for wind stresses τ_x and τ_y. This atmospheric forcing data set is the same that forces the OMCT. Consequently, $\tilde{P}_0$ contains the temporal covariances of τ_x and τ_y that force the ocean model.

The second experiment is called TWO-FORC. The Climate Forecast System Reanalysis (CFSR) [*Saha et al.*, 2010] product from the National Centers for Environmental Prediction (NCEP) is used as an additional atmospheric data set. To estimate the errors, the CFSR and the ERA-Interim wind stresses are subtracted from each other to gain a daily data set of differences between the two reanalysis products. Consequently, $\tilde{P}_0$ contains the temporal covariances of this data set of differences. Unlike the ONE-FORC experiment, the TWO-FORC experiment also accounts for uncertainties that arise from fundamental distinctions between the two reanalysis products.

ONE-FORC and TWO-FORC are extreme cases of a range of error estimation techniques. Both are commonly used [e.g., *Evensen*, 1994; *Pham et al.*, 1998; *Nerger et al.*, 2006; *Saynisch and Thomas*, 2012; *Saynisch et al.*, 2014].

The third experiment is called NO-FORC. In this experiment, it is assumed that the atmospheric forcing is correct, i.e., no source of error is introduced into the modeling by the atmospheric forcing. Therefore, the NO-FORC experiment describes the influence of uncertainties in the oceanic sediments and in the geomagnetic field in the overall error budget. In contrast to ONE-FORC and TWO-FORC, the added term $\sqrt{r+1}V_0C_0^T(\Omega_0^T)^{(\alpha)}$ in equation (4) is set to zero for the wind stress components τ_x and τ_y in all 16 realizations of the state vector x_0^{α}. Consequently, the uncertainties in the wind stresses are neither considered for the spanning of the initial state ensemble, nor during the model propagation.

The entries of the error covariance matrices in each experiment vary due to different estimates of uncertainties in the wind stress components of the atmospheric forcing. To account for possible temporal variations in the wind stress uncertainty, the error covariance matrices are computed on a monthly basis for each experiment. Utilizing a single annual error covariance matrix could lead to a wrong ensemble spread. In this case, uncertainties that are only present during a certain time period of the year can influence the spread of the ensemble over the whole simulation period. A set of monthly error covariance matrices allows to estimate the spatial and temporal (e.g., seasonal) occurrence of uncertainties more flexibly and accurately. Each monthly error covariance matrix is calculated from a 3 month time interval of daily anomalies. For example, the error covariance matrix of January is calculated from the temporal covariances of the time interval December–January–February. A 3 month time interval ensures a sufficiently large sample size for the calculation of the temporal covariances. The time intervals of two consecutive error covariance matrices partly coincide. This overlap ensures a smooth transition between the monthly covariances.

The contribution to the uncertainties in F_z and Σ_{sed} is identical for all three experiments. The covariance of F_z is derived from the secular variation of the ambient geomagnetic field. The influence of the uncertainty in the ambient geomagnetic field is considered to be negligible in the context of this study. *Maus et al.* [2010] estimate a root mean square uncertainty of 1.3 nT for the main geomagnetic field (up to 65,000 nT) and 26 nT/a for the secular variation. The authors state that a significant accumulation of these errors and resulting effect on motional induction in the ocean is only expected for longer time scales, e.g., decadal or millennial time scales. Nevertheless, the uncertainty of F_z is considered in order to ensure consistency of the experiment design. For the sediment conductance, few information are available that can be utilized for
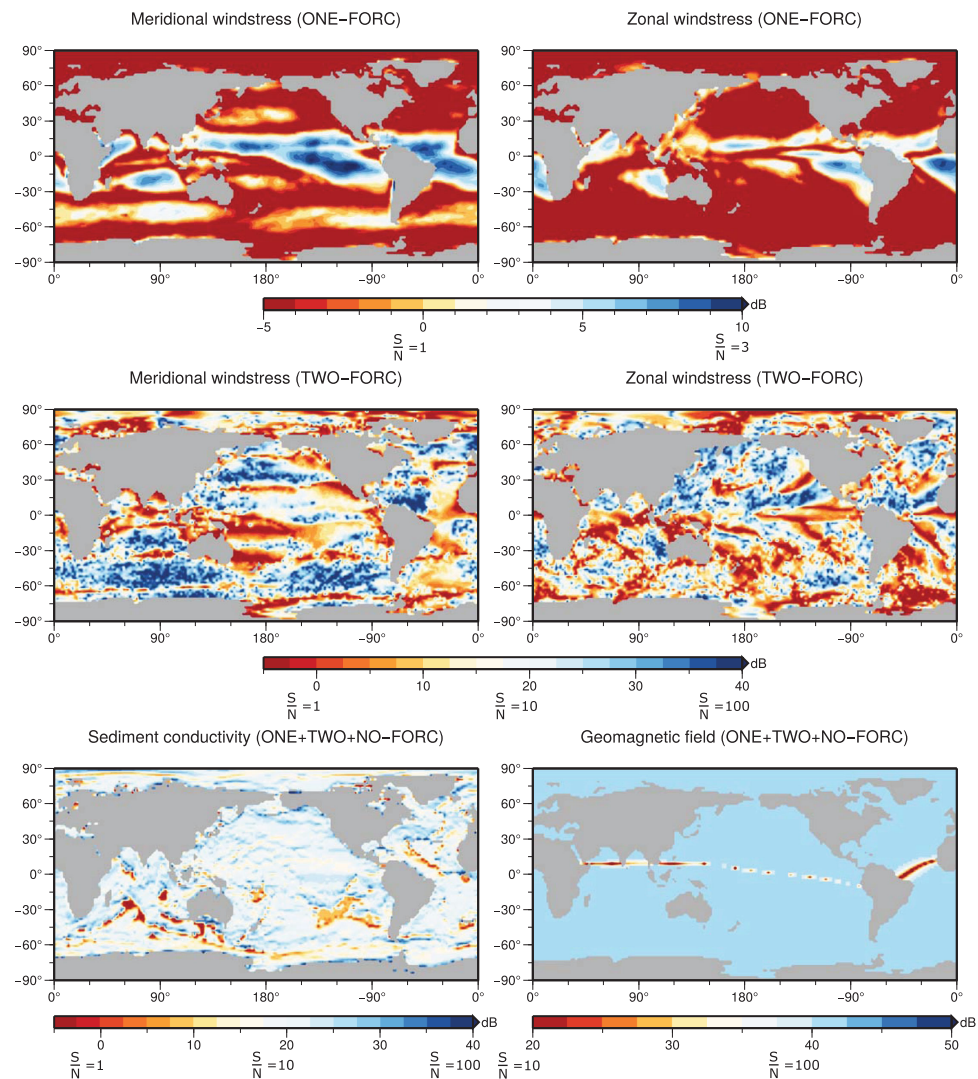
Figure 2. Signal-to-noise ratios (dB) of the estimated uncertainties in the input data used for the January covariance matrices of ONE-FORC, TWO-FORC, and NO-FORC.

estimating the uncertainty. Here five sediment conductivity distributions are mapped to three layers of sediment thicknesses (obtained from *Laske and Masters* [1997]) with respect to the heuristic method described by *Everett et al.* [2003], i.e. (upper layer, middle layer, lower layer): $(0.8, 0.8, 0.02)\,\mathrm{S\,m^{-1}}$, $(0.6, 0.8, 0.02)\,\mathrm{S\,m^{-1}}$, $(0.8, 0.6, 0.02)\,\mathrm{S\,m^{-1}}$, $(0.8, 0.8, 0.01)\,\mathrm{S\,m^{-1}}$ and $(0.7, 0.7, 0.02)\,\mathrm{S\,m^{-1}}$. The results are five different oceanic sediment conductance maps. Next, ten pairwise differences are calculated between the sediment conductance maps. $\tilde{P}_0$ contains the error covariances over these error differences.

The estimated uncertainties in the input data of τ_x, τ_y, F_z, and Σ_{sed} are shown for the January covariance matrices of the ONE-FORC, TWO-FORC, and NO-FORC experiments in Figure 2. The values show signal-to-noise ratios [e.g., *Helstrom et al.*, 2013] between the absolute estimated uncertainty (noise) as described above, and the mean values (signal) of the input data over the 3 month time interval (December–January–February). The signal-to-noise ratios are calculated on a logarithmic scale according to

$$10 \cdot \log_{10}\left(\frac{\text{signal}^2}{\text{noise}^2}\right). \tag{6}$$

In this sense, 0 dB is equivalent to 100% noise, 20 dB is equivalent to 10% noise, and 40 dB is equivalent to 1% noise. In contrast to the calculation of percentage fractions $\frac{\text{noise}}{\text{signal}}$, signal-to-noise ratios circumvent
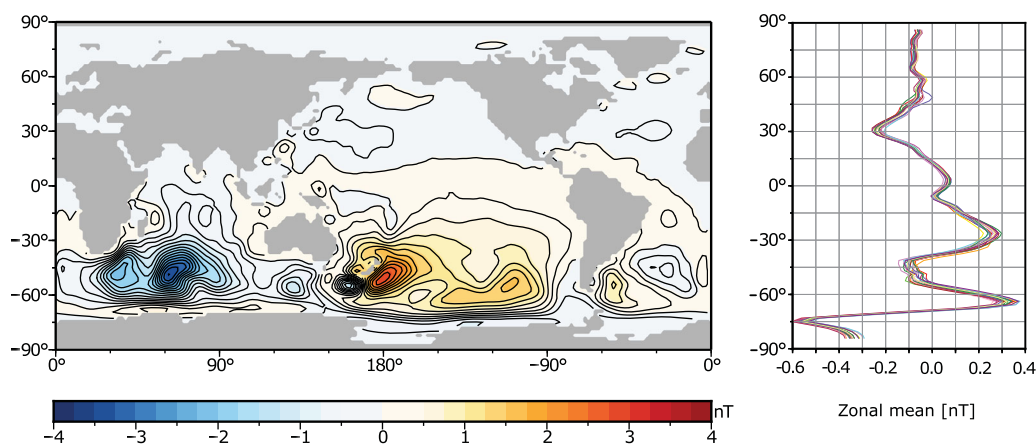
Figure 3. (left) Ensemble mean of the motionally induced magnetic field and (right) zonal mean curves of the 16 motionally induced magnetic field ensemble members of the ONE-FORC experiment. All values are annual mean values at the sea surface (nT).

singularities when the signal strength is equal to zero. On a global scale, the uncertainties in the wind stress of ONE-FORC and TWO-FORC show similar spatial patterns (Figure 2, top and middle). In many regions, the ONE-FORC wind stress uncertainty is 2 orders of magnitude larger than the TWO-FORC uncertainty. Due to the consideration of two different reanalysis data sets, the wind stress uncertainty shows much noisier patterns in TWO-FORC than in ONE-FORC. The estimated wind stress uncertainties derived for the remaining monthly covariance matrices (February–December) differ according to the wind stress dynamics in the respective time intervals. Compared to the wind stress, the uncertainties in the oceanic sediments and in the geomagnetic field are generally low with signal-to-noise ratios mostly below 10% for the oceanic sediments and below 1% for the geomagnetic field (Figure 2, bottom).

Consistent with the atmospheric forcing covariance matrix of January, the uncertainty of the initial state of the OMCT (u, v, S, T) is sampled by the respective covariances from the enclosing time interval December–January–February. The motionally induced magnetic field of each ensemble member and the spread of the ensemble are calculated and stored once per day. The relative amount of uncertainty in the motionally induced magnetic field is calculated by deriving daily signal-to-noise ratios between the ensemble mean of the motionally induced magnetic field (signal) and the ensemble spread (noise).

3. Results and Discussion

3.1. Annual Mean and Maximum Uncertainties

The annual ONE-FORC ensemble mean of the motionally induced magnetic field at the sea surface is depicted in Figure 3 (left). The mean signal strength lies in the range of ± 4 nT and matches with results from previous studies [e.g., *Manoj et al.*, 2006]. The strongest signals are generated by the Antarctic Circumpolar Current in the southern hemisphere. Due to the shape of the radial component of the geomagnetic field of the Earth F_z [e.g., see *Kuvshinov*, 2008, Figure 24], two characteristic large-scale features occur in the South Pacific Ocean (positive values) and in the South Indian Ocean (negative values). To visualize and compare all 16 ensemble members, zonal mean curves are calculated from the 16 annual mean fields. These are depicted in Figure 3 (right) and show the zonally averaged ocean-induced magnetic field of each ensemble member in dependency of the latitude. The zonal mean curves show similar patterns and latitudinal positions of the peak values. However, distinct variations in the peaks of the zonal mean curves are apparent. Additionally, due to the internal dynamics and nonlinearity of the ocean model, the zonal mean curves are not parallel shifted to each other, but strongly interwoven. The zonal mean curves of the ensemble members of the TWO-FORC experiment show similar patterns, but the variations between the zonal mean curves are much smaller (not shown). Hereafter, the causes of these high and low variations in the ONE-FORC and TWO-FORC ensemble spreads are discussed, as well as their spatial distribution and temporal evolution.
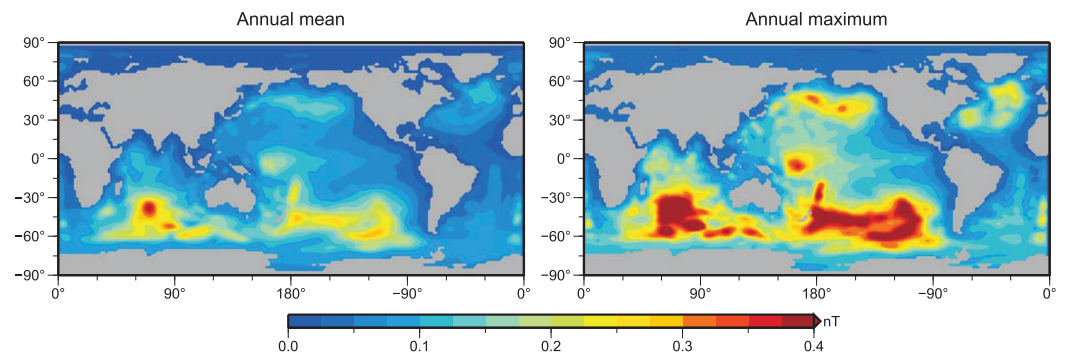
Figure 4. (left) Annual mean and (right) annual maximum ONE-FORC ensemble spread (nT) of the motionally induced magnetic field.

The annual mean and maximum ensemble spreads of the ONE-FORC and the TWO-FORC experiments are shown in Figures 4 and 5. For the sake of comparability, the mean and maximum plots are shown using the same color bar that originates from the respective annual mean value range.

The annual mean ONE-FORC ensemble spread of the motionally induced magnetic field ranges from 0 to 0.4 nT. The highest values occur in the area of the Antarctic Circumpolar Current. More specifically, the areas with the largest ensemble spread occur where also the largest magnetic field strength is generated (compare the left plots of Figures 3 and 4). In the South Pacific Ocean and the South Indian Ocean, large-scale patterns with an ensemble spread between 0.2 and 0.4 nT are visible. Additional features in the range of 0.1 and 0.2 nT occur in the Indian Ocean, east and north-east of Australia, in the North Pacific Ocean (between 30°N and 60°N) and in the North Atlantic Ocean. As shown in Figure 4, the annual mean and maximum values of the ONE-FORC ensemble spread show similar features. However, the values of the annual maximum ensemble spread are much higher and range from 0 to 0.7 nT. Again, the peak values are found in the area of the Antarctic Circumpolar Current with values between 0.3 and 0.7 nT in the South Indian Ocean and between 0.3 and 0.5 nT in the South Pacific Ocean. The features in the Indian Ocean, east and north-east of Australia, in the North Pacific Ocean, and in the North Atlantic Ocean also show relatively high values in the range of 0.25–0.35 nT.

The annual mean and maximum TWO-FORC ensemble spreads show much lower values and different spatial patterns as compared to the ONE-FORC experiment (see Figures 4 and 5). The annual mean ensemble spread of the motionally induced magnetic field ranges from 0 to 0.1 nT. As in the ONE-FORC experiment, the highest values occur in the Antarctic Circumpolar Current. In contrast to the spatial distribution of the ensemble spread in the ONE-FORC experiment (Figure 4, left), the spatial features on the northern hemisphere and in the equatorial region are much more prominent when compared to the strongest features in the area of the Antarctic Circumpolar Current (Figure 5, left). This becomes even more apparent when comparing the annual maximum ensemble spreads of the ONE-FORC and TWO-FORC experiments (right plots of Figures 4 and 5). The strongest features of the maximum TWO-FORC ensemble spread range from 0.1 to 0.15 nT in the western and southern Pacific Ocean and from 0.1 to 0.2 nT in the South Indian Ocean.
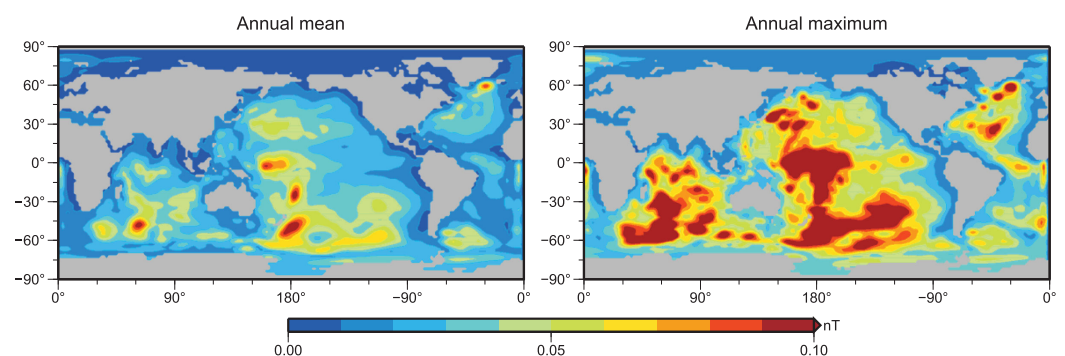

Figure 5. (left) Annual mean and (right) annual maximum TWO-FORC ensemble spread (nT) of the motionally induced magnetic field.
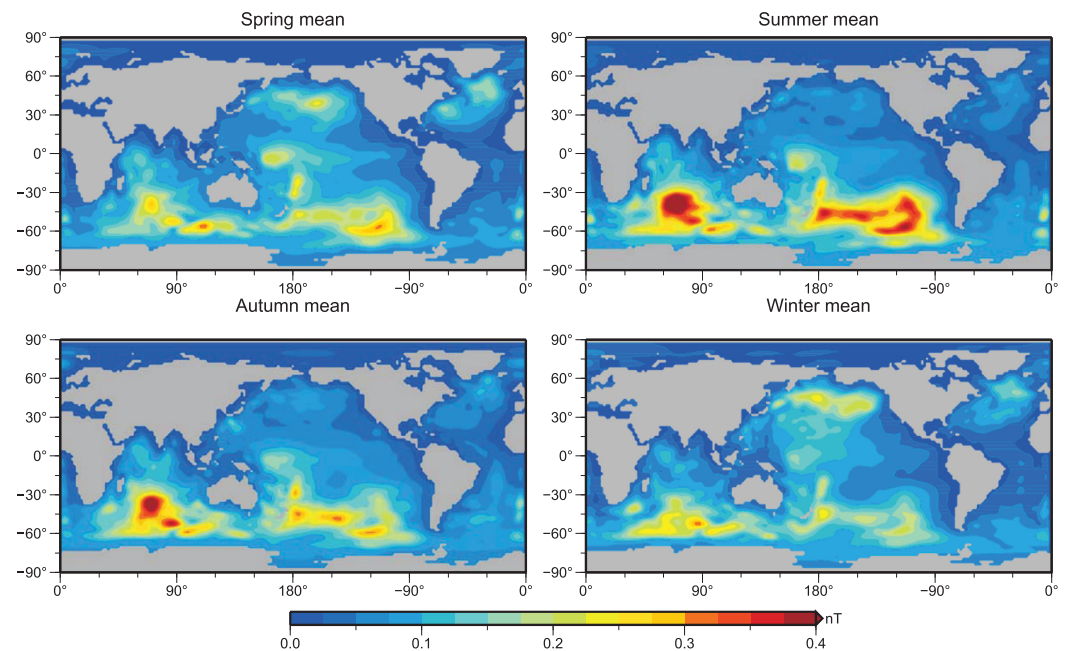
Figure 6. Seasonal mean ONE-FORC ensemble spread (nT) of the motionally induced magnetic field.

In the NO-FORC experiment, the results show only a marginal ensemble spread of the motionally induced magnetic field (not shown). This corresponds to a small influence of the combined uncertainties in the oceanic sediments and in the geomagnetic field on the ocean-induced magnetic field. In many areas, the NO-FORC ensemble spread is 1 order of magnitude smaller than the TWO-FORC ensemble spread. High-value patterns in the NO-FORC ensemble spread lie in the range of 0.02–0.05 nT. In comparison to ONE-FORC and TWO-FORC, the NO-FORC ensemble spread is considered to be negligible.

As a result, it is concluded that uncertainties in the wind stress components of the atmospheric forcing are the major source of the uncertainties in the motionally induced magnetic field (with respect to the considered error budgets, as described in section 2.3).

The differences in the strength and spatial patterns between the ONE-FORC and the TWO-FORC experiments can be explained by the different assumptions for the calculation of the error covariance matrices (see section 2.3 and Figure 2). In the ONE-FORC experiment, the uncertainty in the wind stress is approximated by the temporal variances and covariances of the respective time series. As a consequence, the introduced uncertainties are probably overestimated. In the TWO-FORC experiment, the error covariances are based on the differences between the CFSR and ERA-Interim atmospheric forcing data sets. Ideally, these differences account for various uncertainties in the wind stresses, e.g., errors in the atmospheric modeling, errors due to numerical schemes, errors due to different spatiotemporal availability of observational data, or errors due to different data assimilation schemes. Both the ERA-Interim and the CFSR data sets are reanalysis products that merge atmospheric models and observations. The observations are assimilated by a 4DVar scheme into the ERA-Interim product [*Dee et al.*, 2011] and by a 3DVar scheme into the CFSR product [*Saha et al.*, 2010]. *Decker et al.* [2012] have shown that the two reanalysis products exhibit many differences on varying spatiotemporal scales and, in particular, at regional spatial scales. In principle, large uncertainties in specific regions in the atmospheric forcing can create large uncertainties in the ocean circulation patterns in the respective regions [*Chaudhuri et al.*, 2013]. However, on a global scale and during the considered time scales in this study, the differences between ERA-Interim and CFSR wind stresses in the TWO-FORC experiment lead to a small ensemble spread of the motionally induced magnetic field. The consideration of additional atmospheric forcing data sets could further enhance the error budget and cover more error sources. In this context, the TWO-FORC ensemble spread probably provides an underestimated uncertainty in the motionally induced magnetic field. In summary, it can be concluded that the ONE-FORC and TWO-FORC experiments yield first upper and lower limits (i.e., a reasonable range) of the uncertainty in the motionally induced magnetic field.
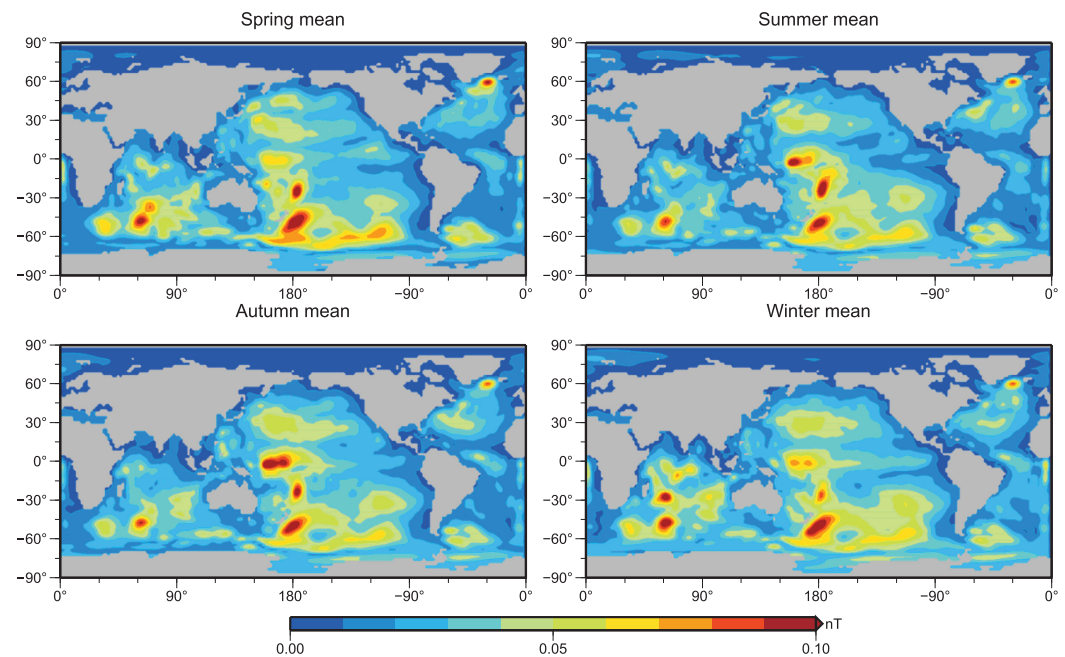
Figure 7. Seasonal mean TWO-FORC ensemble spread (nT) of the motionally induced magnetic field.

3.2. Seasonal Variations in the Uncertainties

The effect of annual and seasonal variations in the introduced uncertainty can also be investigated. The seasonal variations of the ONE-FORC and TWO-FORC ensemble spreads are depicted in Figures 6 and 7. The four plots show mean values over 3 month intervals that are calculated from the daily ensemble spread time series (spring: March–April–May, summer: June–July–August, autumn: September–October–November, and winter: December–January–February).

The ONE-FORC ensemble spread and its spatial distribution show large seasonal variations (Figure 6). The largest values occur in the area of the Antarctic Circumpolar Current during the summer season. Two major patterns are apparent in the South Indian Ocean and in the South Pacific Ocean. In the South Indian Ocean, peak values of up to 0.6 nT occur. In the South Pacific Ocean, the major pattern shows values between 0.2 and 0.4 nT. During the autumn season, the mean ONE-FORC ensemble spread shows a general decrease in the southern hemisphere. The major feature in the South Indian Ocean is still visible and reaches peak values of up to 0.5 nT. In the South Pacific Ocean, peak values up to 0.3 nT occur. The lowest ONE-FORC ensemble spread in the southern hemisphere occurs during the winter season. The major feature that is visible in the South Indian Ocean during the summer and autumn seasons is absent in the winter season. The highest values reach up to 0.3 nT in the South Indian Ocean and up to 0.2 nT in the South Pacific Ocean. In the spring season, the mean ONE-FORC ensemble spread increases again. In contrast to the seasonal changes in the southern hemisphere, the mean ONE-FORC ensemble spread shows converse seasonal variations on the northern hemisphere. The lowest mean ONE-FORC ensemble spread is apparent during the summer season with peak values below 0.1 nT. The highest mean ONE-FORC ensemble spread is visible during the winter season with peak values up to 0.2 nT in the North Pacific Ocean. In summary, the ONE-FORC ensemble spread shows distinct seasonal variations with peak values during the summer season in the southern hemisphere (ACC region) and during the winter season on the northern hemisphere (Kuroshio region).

The TWO-FORC ensemble spread shows a much more static behavior in both the seasonal variations and its spatial distribution (Figure 7). The values for all seasons lie in a comparable range of up to 0.1 nT. In all four seasons, similar patterns with peak values up to 0.1 nT are visible in the South Indian Ocean, south-east of Greenland, and north-east, east, and south-east of Australia. Additional features with values around 0.05 nT are visible throughout all seasons in the Indian Ocean, West Pacific Ocean, South-east Pacific Ocean, North Atlantic Ocean, and east of the Drake passage.
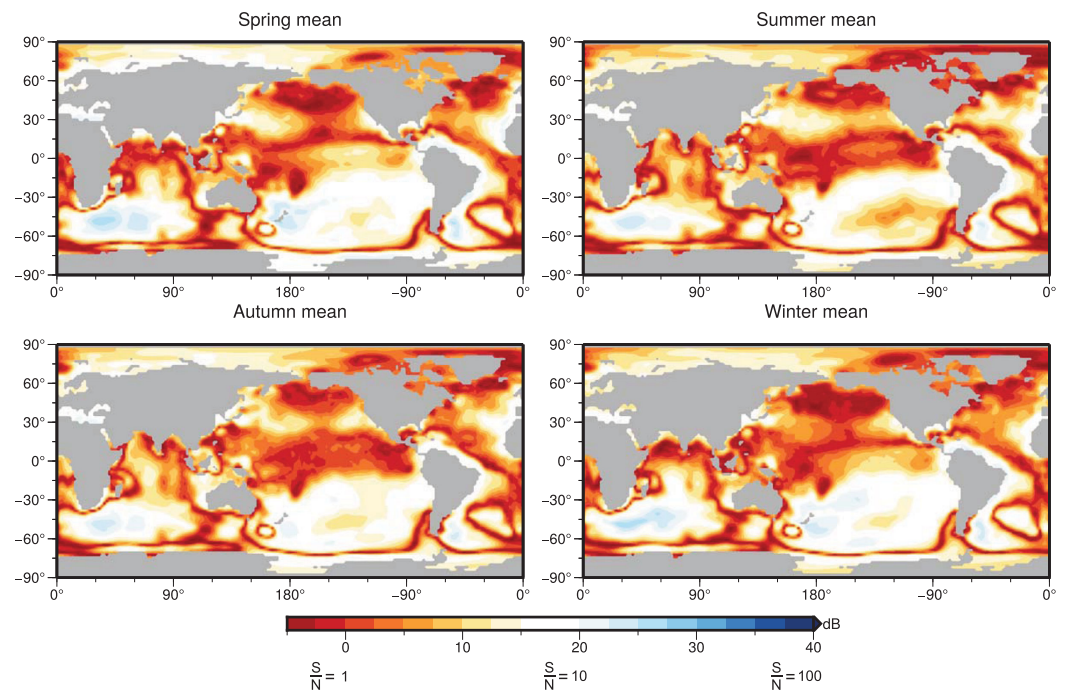
Figure 8. Seasonal mean ONE-FORC signal-to-noise ratio (dB) of the motionally induced magnetic field signal (S) and the ensemble spread (N).

3.3. Signal-to-Noise Ratios of the Motional Induction

In order to put the previously described absolute uncertainty in relation to the motionally induced magnetic field, daily signal-to-noise ratios of the signal strength (Figure 3, left) and the ensemble spreads (Figures 6 and 7) are calculated as described in section 2.3. The signal-to-noise ratios of the ONE-FORC and TWO-FORC experiments are shown in Figures 8 and 9. In accordance with the seasonal depiction of
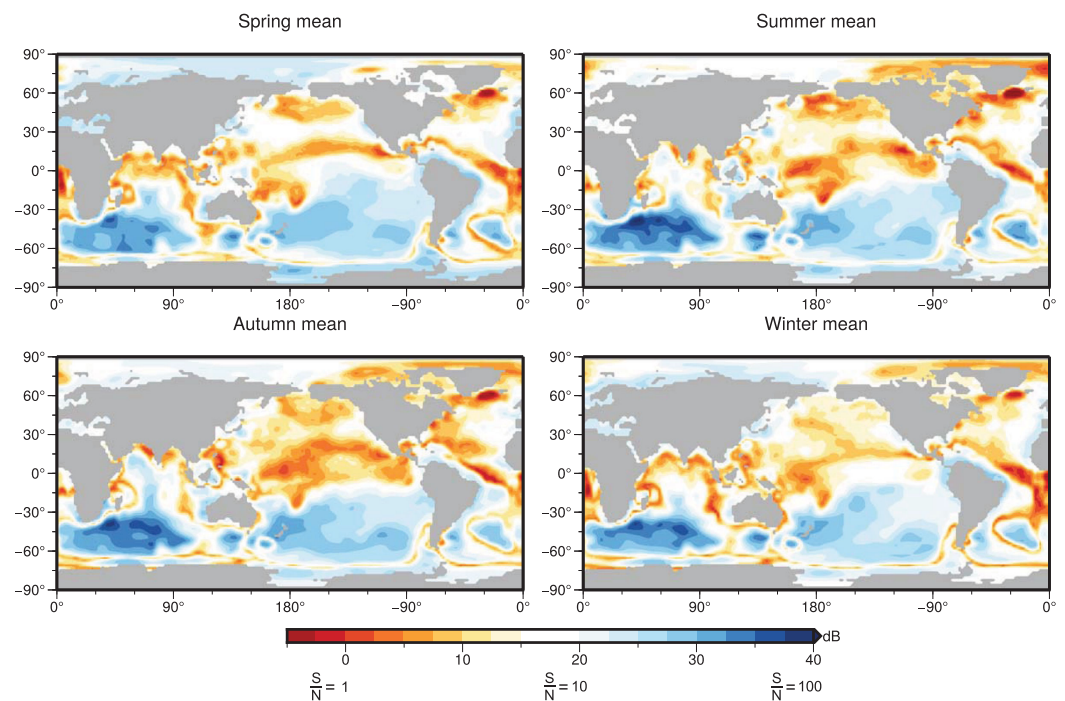
Figure 9. Seasonal mean TWO-FORC signal-to-noise ratio (dB) of the motionally induced magnetic field signal (S) and the ensemble spread (N).

the ONE-FORC and TWO-FORC ensemble spreads, the signal-to-noise ratios also are subdivided into four seasonal mean maps. Both figures show signal-to-noise ratios of up to 40 dB on a logarithmic scale. High values correspond to a low fraction of noise in the signal, i.e., a small relative ensemble spread. The chosen maximum value of 40 dB corresponds to a signal-to-noise ratio of 100, i.e., a relative uncertainty of 1% in the motionally induced magnetic field. Negative values indicate areas where the ensemble spread is larger than the signal strength.

On a global scale, the seasonal mean ONE-FORC and TWO-FORC signal-to-noise ratios show a distinct partition with low values on the northern hemisphere and high values in the southern hemisphere. This pattern can be explained by the structure of the ocean global circulation induced magnetic field (Figure 3). In particular, the two major features of the motionally induced magnetic field are visible as high-value regions in the South Indian Ocean and in the South Pacific Ocean (compare Figure 3 with Figures 8 and 9). In these areas, the highest signal-to-noise ratios occur.

The highest ONE-FORC signal-to-noise ratios lie in the range from 15 to 25 dB in the South Indian Ocean and from 10 to 25 dB in the South Pacific Ocean (Figure 8). The lowest ONE-FORC signal-to-noise ratios in the range of −5 to 10 dB occur in equatorial regions, North Indian Ocean, North Pacific Ocean, and North Atlantic Ocean. Some regions gain particular interest, as they retain a signal-to-noise ratio of around 20 dB or higher throughout all seasons, i.e., in the South Indian Ocean, around Japan, in the South Pacific Ocean around New Zealand, in the Mediterranean Sea, and east of the Drake Passage.

As described in section 3.2, the TWO-FORC ensemble spread is much smaller than the ONE-FORC ensemble spread. Consequently, higher TWO-FORC signal-to-noise ratios occur in all regions (Figure 9). Peak values in the range of 25–40 dB are found to occur in the South Indian Ocean, South Pacific Ocean, and South Atlantic Ocean. These patterns show a general match with the areas of highest ONE-FORC signal-to-noise ratios in the southern hemisphere. Large-scale features with a low signal-to-noise ratio in the range between 5 and 15 dB are visible in the North Indian Ocean, northern equatorial region of the Atlantic and Pacific Ocean, North Pacific Ocean, and south-east of Greenland. As in the ONE-FORC experiment, some regions retain a low uncertainty throughout the year, e.g., in the South Indian Ocean, in the area of the Kuroshio Current, in the South Pacific Ocean, east of the Drake Passage, and in the South Atlantic Ocean.

The presented results reveal spatiotemporal patterns that are either highly or minimally sensitive toward the introduced uncertainties. Although the ONE-FORC and TWO-FORC ensemble spreads (Figures 6 and 7) show by far the largest range in the area of the Antarctic Circumpolar Current, the ONE-FORC and TWO-FORC signal-to-noise ratios show the lowest amount of noise in these areas (Figures 8 and 9). The exact opposite is found in many regions on the northern hemisphere. These results are due to the spatial distribution of the signal strength of the motionally induced magnetic field (Figure 3). The Antarctic Circumpolar Current is the strongest ocean current and generates the largest magnetic signals (Figure 3). In turn, the large ONE-FORC ensemble spread in these areas (Figure 4) result in a large signal-to-noise ratio of the magnetic field. On the contrary, even the small TWO-FORC ensemble spread (Figure 5) results in a considerable small signal-to-noise ratio of the magnetic field on the northern hemisphere (Figure 9).

The results of this study suggest that the aggregated influence of the various introduced uncertainties on motional induction in the ocean is very diverse. However, despite the varying assumptions for the uncertainty in the atmospheric forcing, the ONE-FORC and TWO-FORC experiments show coinciding regions where the signal-to-noise ratios remain either large or small throughout all seasons. These regions are identified as either nonsensitive or sensitive toward the introduced uncertainties. Especially the nonsensitive areas, i.e., regions in which the uncertainty in the motionally induced magnetic field remains low, are of interest. Regions in which the modeled motionally induced magnetic field is found reliable (within uncertainty limits) allows the most reasonable comparison with observational data. Also the assimilation of observational data into a model is most promising in regions of a low and well-known uncertainty. As described in section 3.1, the derived ONE-FORC and TWO-FORC uncertainties describe upper and lower limits of a realistic range of the uncertainties. In the setting of this study, the main contribution is caused by the wind stress from the atmospheric forcing. To further narrow the presented range of uncertainties, additional constraints for the error budgets in the atmospheric forcing need to be included in the error covariance matrices.

4. Summary and Conclusion

The modeling of the ocean global circulation induced magnetic field is affected by various errors that are introduced through input data and modeling deficiencies. In this study, ensemble simulations over one annual cycle are carried out to estimate the uncertainty in the modeling of the magnetic field that is induced by ocean global circulation. Both spatial patterns and seasonal variations of the uncertainty in the so-called motionally induced magnetic field are investigated. Furthermore, distinct regions are identified in the motionally induced magnetic field, which are only minimally sensitive toward introduced uncertainties.

To calculate the motionally induced magnetic field, a one-sided coupling of an ocean global circulation model and an electromagnetic induction model is used. The initial state and its prescribed uncertainty are assumed to resemble a normal probability density distribution, which is sampled by an ensemble of model realizations. The ensemble mean and spread are generated systematically and approximate the error statistics of the initial probability density distribution. To span this ensemble, error covariance matrices are calculated, which account for error budgets in zonal ocean flow velocity, meridional ocean flow velocity, zonal wind stress, meridional wind stress, ocean temperature, salinity, radial component of the ambient geomagnetic field, and oceanic sediment conductance. The analysis of the ensemble spread allows to investigate the aggregated effect of the introduced uncertainties on the motional induction. In addition, the predominant source of uncertainty is identified.

The global annual mean ensemble spread of the motionally induced magnetic field ranges from 0.1 to 0.4 nT. The largest mean values occur in the area of the Antarctic Circumpolar Current, especially in South Indian Ocean and in the South Pacific Ocean. The largest annual maximum ensemble spread reaches values in the range of 0.2–0.7 nT in the South Indian Ocean. In the South Pacific Ocean, the largest annual maximum ensemble spread reaches values in the range of 0.15–0.5 nT. In these areas, the relative amount of uncertainty (signal-to-noise ratio between the signal strength of the motionally induced magnetic field and its ensemble spread) lies in the range of 1%–10%. However, on the northern hemisphere, the overall smaller ensemble spreads result in much higher signal-to-noise ratios. In particular, large-scale regions with signal-to-noise ratios of 30% or higher occur in the North Indian Ocean, North Pacific Ocean, and North Atlantic Ocean. The described range of uncertainty in the motionally induced magnetic field is found to predominantly originate from the uncertainty in the wind stresses that force the wind-driven ocean circulation.

The experiments demonstrate that the motionally induced magnetic field reacts very sensitively toward introduced uncertainties. Nevertheless, some regions appear to be minimally sensitive, i.e., a small uncertainty is retained throughout all simulation experiments. These regions are found to occur in the South Indian Ocean, South Pacific Ocean, around Japan, and in the South Atlantic Ocean.

Motionally induced magnetic fields may be utilized as indirect observations of ocean global circulation. To understand the spatiotemporal behavior of the induced magnetic field, the numerical modeling of this process is essential. This study highlights that the modeling of motional induction due to ocean global circulation is subject to various errors. For many applications, the knowledge about uncertainties in the modeling is crucial, e.g., the comparison of observational data and model results, or for data assimilation purposes. In this context, the revealed minimally sensitive patterns in the oceanic induced magnetic field may serve as candidate regions for promising future studies of motional induction in the ocean. The inclusion of additional error budgets may further constrain the range of a realistic estimation of the uncertainty in the motionally induced magnetic field (e.g., error information on conductivity structures in the mantle of the Earth).

References

Chaudhuri, A. H., R. M. Ponte, G. Forget, and P. Heimbach (2013), A comparison of atmospheric reanalysis surface products over the ocean and implications for uncertainties in air–sea boundary forcing, *J. Clim.*, *26*(1), 153–170, doi:10.1175/JCLI-D-12-00090.1.

Chave, A. D. (1983), On the theory of electromagnetic induction in the Earth by ocean currents, *J. Geophys. Res.*, *88*(B4), 3531–3542, doi: 10.1029/JB088iB04p03531.

Chave, A. D., and D. S. Luther (1990), Low-frequency, motionally induced electromagnetic fields in the ocean: 1. Theory, *J. Geophys. Res.*, *95*(C5), 7185–7200.

Cox, C. S. (1980), Electromagnetic induction in the oceans and interferences on the constitution of the earth, *Surv. Geophys.*, *4*, 137–156, doi:10.1007/BF01452963.

Decker, M., M. A. Brunke, Z. Wang, K. Sakaguchi, X. Zeng, and M. G. Bosilovich (2012), Evaluation of the reanalysis products from GSFC, NCEP, and ECMWF using flux tower observations, *J. Clim.*, *25*(6), 1916–1944, doi:10.1175/JCLI-D-11-00004.1.

Dee, D. P., et al. (2011), The ERA-Interim reanalysis: Configuration and performance of the data assimilation system, *Q. J. R. Meteorol. Soc.*, *137*(656), 553–597, doi:10.1002/qj.828.

Dobslaw, H., and M. Thomas (2007), Simulation and observation of global ocean mass anomalies, *J. Geophys. Res.*, *112*, C05040, doi:10.1029/2006JC004035.

Dobslaw, H., F. Flechtner, I. Bergmann-Wolf, C. Dahle, R. Dill, S. Esselborn, I. Sasgen, and M. Thomas (2013), Simulating high-frequency atmosphere-ocean mass variability for dealiasing of satellite gravity observations: AOD1B RL05, *J. Geophys. Res.*, *118*, 3704–3711, doi:10.1002/jgrc.20271.

Dostal, J., Z. Martinec, and M. Thomas (2012), The modelling of the toroidal magnetic field induced by tidal ocean circulation, *Geophys. J. Int.*, *189*(2), 782–798, doi:10.1111/j.1365-246X.2012.05407.x.

Driscoll, J. R., and D. M. Healy (1994), Computing Fourier transforms and convolutions on the 2-sphere, *Adv. Appl. Math.*, *15*, 202–250, doi:10.1006/aama.1994.1008.

Evensen, G. (1994), Inverse methods and data assimilation in nonlinear ocean models, *Physica D*, *77*(1–3), 108–129, doi:10.1016/0167-2789(94)90130-9.

Everett, M. E., S. Constable, and C. G. Constable (2003), Effects of near-surface conductance on global satellite induction responses, *Geophys. J. Int.*, *153*(1), 277–286, doi:10.1046/j.1365-246X.2003.01906.x.

Flosadóttir, A. H., J. C. Larsen, and J. T. Smith (1997), Motional induction in North Atlantic circulation models, *J. Geophys. Res.*, *102*(C5), 10,353–10,372, doi:10.1029/96JC03603.

Greatbatch, R. J. (1994), A note on the representation of steric sea level in models that conserve volume rather than mass, *J. Geophys. Res.*, *99*(C6), 12,767–12,771, doi:10.1029/94JC00847.

Helstrom, C., D. Fry, L. Costrell, and K. Kandiah (2013), *Statistical Theory of Signal Detection: International Series of Monographs in Electronics and Instrumentation, Int. Ser. Monogr. Electron. Instrum.*, Elsevier Sci., Amsterdam, Netherlands.

Irrgang, C., J. Saynisch, and M. Thomas (2016), Impact of variable seawater conductivity on motional induction simulated with an ocean general circulation model, *Ocean Sci.*, *12*, 129–136, doi:10.5194/os-12-129-2016.

Jakobson, E., T. Vihma, T. Palo, L. Jakobson, H. Keernik, and J. Jaagus (2012), Validation of atmospheric reanalyses over the central Arctic Ocean, *Geophys. Res. Lett.*, *39*, L10802, doi:10.1029/2012GL051591.

Kim, J.-E., and M. J. Alexander (2013), Tropical precipitation variability and convectively coupled equatorial waves on submonthly time scales in reanalyses and TRMM, *J. Clim.*, *26*(10), 3013–3030, doi:10.1175/JCLI-D-12-00353.1.

Kuvshinov, A. (2008), 3-D global induction in the oceans and solid earth: Recent progress in modeling magnetic and electric fields from sources of magnetospheric, ionospheric and oceanic origin, *Surv. Geophys.*, *29*(2), 139–186, doi:10.1007/s10712-008-9045-z.

Kuvshinov, A., T. Sabaka, and N. Olsen (2006), 3-D electromagnetic induction studies using the Swarm constellation: Mapping conductivity anomalies in the Earth's mantle, *Earth Planets Space*, *58*, 417–427, doi:10.1186/BF03351938.

Larsen, J. C. (1968), Electric and magnetic fields induced by deep sea tides, *Geophys. J. R. Astron. Soc.*, *16*, 47–70, doi:10.1111/j.1365-246X.1968.tb07135.x.

Laske, G., and G. Masters (1997), A global digital map of sediment thickness, *Eos Trans. AGU*, *78*(46), Fall Meet. Suppl., F483.

Lilley, F. E. M., J. H. Filloux, P. J. Mulhearn, and I. J. Ferguson (1993), Magnetic signals from an ocean eddy, *J. Geomagn. Geoelectr.*, *45*(5), 403–422, doi:10.5636/jgg.45.403.

Lowes, F. J. (2000), An estimate of the errors of the IGRF/DGRF fields 1945–2000, *Earth Planets Space*, *52*(12), 1207–1211, doi:10.1186/BF03352353.

Manoj, C., A. Kuvshinov, S. Maus, and H. Lühr (2006), Ocean circulation generated magnetic signals, *Earth Planets Space*, *58*(4), 429–437, doi:10.1186/BF03351939.

Maus, S., and A. Kuvshinov (2004), Ocean tidal signals in observatory and satellite magnetic measurements, *Geophys. Res. Lett.*, *31*, L15313, doi:10.1029/2004GL020090.

Maus, S., C. Manoj, J. Rauberg, I. Michaelis, and H. Lühr (2010), NOAA/NGDC candidate models for the 11th generation International Geomagnetic Reference Field and the concurrent release of the 6th generation Pomme magnetic model, *Earth Planets Space*, *62*(10), 729–735, doi:10.5047/eps.2010.07.006.

Nerger, L., W. Hiller, and J. Schröter (2005), A comparison of error subspace Kalman filters, *Tellus, Ser. A*, *57*(5), 715–735, doi:10.1111/j.1600-0870.2005.00141.x.

Nerger, L., S. Danilov, W. Hiller, and J. Schröter (2006), Using sea-level data to constrain a finite-element primitive-equation ocean model with a local SEIK filter, *Ocean Dyn.*, *56*(5–6), 634–649, doi:10.1007/s10236-006-0083-0.

Nerger, L., S. Danilov, G. Kivman, W. Hiller, and J. Schröter (2007), Data assimilation with the ensemble Kalman filter and the SEIK filter applied to a finite element model of the North Atlantic, *J. Mar. Syst.*, *65*(1–4), 288–298, doi:10.1016/j.jmarsys.2005.06.009.

Parkinson, W. D., and V. R. S. Hutton (1989), *The Electrical Conductivity of the Earth*, vol. 3, pp. 261–232, Academic, San Diego, Calif.

Pham, D. T. (2001), Stochastic methods for sequential data assimilation in strongly nonlinear systems, *Mon. Weather Rev.*, *129*, 1194–1207, doi:10.1175/1520-0493(2001)129 < 1194:SMFSDA>2.0.CO;2.

Pham, D. T., J. Verron, and M. Christine Roubaud (1998), A singular evolutive extended Kalman filter for data assimilation in oceanography, *J. Mar. Syst.*, *16*(3–4), 323–340, doi:10.1016/S0924-7963(97)00109-7.

Sabaka, T. J., N. Olsen, R. H. Tyler, and A. Kuvshinov (2015), CM5, a pre-Swarm comprehensive geomagnetic field model derived from over 12 yr of CHAMP, Orsted, SAC-C and observatory data, *Geophys. J. Int.*, *200*(3), 1596–1626, doi:10.1093/gji/ggu493.

Saha, S., et al. (2010), The NCEP climate forecast system reanalysis, *Bull. Am. Meteorol. Soc.*, *91*(8), 1015–1057, doi:10.1175/2010BAMS3001.1.

Sanford, T. B. (1971), Motionally induced electric and magnetic fields in the sea, *J. Geophys. Res.*, *76*(15), 3476–3492, doi:10.1029/JC076i015p03476.

Saynisch, J., and M. Thomas (2012), Ensemble Kalman-filtering of Earth rotation observations with a global ocean model, *J. Geodyn.*, *62*, 24–29, doi:10.1016/j.jog.2011.10.003.

Saynisch, J., I. Bergmann-Wolf, and M. Thomas (2014), Assimilation of GRACE-derived oceanic mass distributions with a global ocean circulation model, *J. Geod.*, *89*(2), 121–139, doi:10.1007/s00190-014-0766-0.

Schnepf, N. R., C. Manoj, A. Kuvshinov, H. Toh, and S. Maus (2014), Tidal signals in ocean-bottom magnetic measurements of the Northwestern Pacific: Observation versus prediction, *Geophys. J. Int.*, *198*(2), 1096–1110, doi:10.1093/gji/ggu190.

Schnepf, N. R., A. Kuvshinov, and T. Sabaka (2015), Can we probe the conductivity of the lithosphere and upper mantle using satellite tidal magnetic signals?, *Geophys. Res. Lett.*, *42*, 3233–3239, doi:10.1002/2015GL063540.

Stephenson, D., and K. Bryan (1992), Large-scale electric and magnetic fields generated by the oceans, *J. Geophys. Res.*, *97*(C10), 15,467–15,480, doi:10.1029/92JC01400.

Szuts, Z. B. (2010), Relationship between ocean velocity and motionally induced electrical signals: 2. In the presence of sloping topography, *J. Geophys. Res.*, *115*, C06004, doi:10.1029/2009JC006054.

Thébault, E., et al. (2015), Evaluation of candidate geomagnetic field models for IGRF-12, *Earth Planets Space*, *67*(1), 112, doi:10.1186/s40623-015-0273-4.

Thomas, M., J. Sündermann, and E. Maier-Reimer (2001), Consideration of ocean tides in an OGCM and impacts on subseasonal to decadal polar motion excitation, *Geophys. Res. Lett.*, *28*(12), 2457–2460, doi:10.1029/2000GL012234.

Tyler, R. H., L. A. Mysak, and J. M. Oberhuber (1997), Electromagnetic fields generated by a three dimensional global ocean circulation, *J. Geophys. Res.*, *102*(C3), 5531–5551, doi:10.1029/96JC03545.

Tyler, R. H., S. Maus, and H. Lühr (2003), Satellite observations of magnetic fields due to ocean tidal flow, *Science*, *299*(5604), 239–241, doi:10.1126/science.1078074.

Vennerstrom, S., E. Friis-Christensen, H. Lühr, T. Moretto, N. Olsen, C. Manoj, P. Ritter, L. Rastätter, A. Kuvshinov, and S. Maus (2005), The impact of combined magnetic and electric field analysis and of ocean circulation effects on swarm mission performance, technical report, Dan. Natl. Space Cent., Kgs. Lyngby, Denmark.

Vivier, F., E. Meier-Reimer, and R. H. Tyler (2004), Simulations of magnetic fields generated by the Antarctic Circumpolar Current at satellite altitude: Can geomagnetic measurements be used to monitor the flow?, *Geophys. Res. Lett.*, *31*, L10306, doi:10.1029/2004GL019804.